

## Star-gas misalignment in galaxies: I. the properties of galaxies from the Horizon-AGN simulation and comparisons to SAMI

DONGHYEON J. KHM<sup>1</sup>, SUKYOUNG K. YI<sup>1</sup>, YOHAN DUBOIS<sup>2</sup>, JULIA J. BRYANT<sup>3, 4, 5</sup>, CHRISTOPHE PICHON<sup>2, 6</sup>, SCOTT M. CROOM<sup>3, 5</sup>, JOSS BLAND-HAWTHORN<sup>3</sup>, SARAH BROUUGH<sup>7</sup>, HOSEUNG CHOI<sup>8</sup>, JULIEN DEVRIENDT<sup>9</sup>, BRENT GROVES<sup>10, 11</sup>, MATT S. OWERS<sup>12, 13</sup>, SAMUEL N. RICHARDS<sup>14</sup>, JESSE VAN DE SANDE<sup>3, 5</sup>, AND SARAH M. SWEET<sup>5, 15</sup>

<sup>1</sup>Department of Astronomy, Yonsei University, Seoul 03722, Republic of Korea

<sup>2</sup>Institut d Astrophysique de Paris, Sorbonne Universit<sup>es</sup>, et CNRS, UMP 7095, 98 bis bd Arago, 75014 Paris, France

<sup>3</sup>Sydney Institute for Astronomy (SI<sup>A</sup>), School of Physics, The University of Sydney, NSW 2006, Australia

<sup>4</sup>Australian Astronomical Optics, AAO-USydney, School of Physics, University of Sydney, NSW 2006, Australia

<sup>5</sup>ARC Centre of Excellence for All Sky Astrophysics in 3 Dimensions (ASTRO 3D)

<sup>6</sup>Korea Institute of Advanced Studies (KIAS), 85 Hoegiro, Dongdaemun-gu, Seoul, 02455, Republic of Korea

<sup>7</sup>School of Physics, University of New South Wales, NSW 2052, Australia

<sup>8</sup>Institute of Theoretical Astrophysics, University of Oslo, Oslo, Norway

<sup>9</sup>Dept of Physics, University of Oxford, Keble Road, Oxford OX1 3RH, UK

<sup>10</sup>International Centre for Radio Astronomy Research (ICRAR), University of Western Australia, Crawley, WA 6009, Australia

<sup>11</sup>Research School of Astronomy & Astrophysics, Australian National University, Weston Creek, ACT, 2611, Australia

<sup>12</sup>Department of Physics and Astronomy, Macquarie University, NSW 2109, Australia

<sup>13</sup>Astronomy, Astrophysics and Astrophotonics Research Centre, Macquarie University, Sydney, NSW 2109, Australia

<sup>14</sup>SOFIA Science Center, USRA, NASA Ames Research Center, Building N232, M/S 232-12, P.O. Box 1, Moffett Field, CA 94035-0001, USA

<sup>15</sup>Centre for Astrophysics and Supercomputing, Swinburne University of Technology, PO Box 218, Hawthorn, VIC 3122, Australia

(Received November 15, 2019; Revised XX; Accepted XX)

Submitted to ApJ

### ABSTRACT

Recent integral field spectroscopy observations have found that about 11% of galaxies show star-gas misalignment. The misalignment possibly results from external effects such as gas accretion, interaction with other objects, and other environmental effects, hence providing clues to these effects. We explore the properties of misaligned galaxies using Horizon-AGN, a large-volume cosmological simulation, and compare the result with the result of the Sydney-AAO Multi-object integral field spectrograph (SAMI) Galaxy Survey. Horizon-AGN can match the overall misalignment fraction and reproduces the distribution of misalignment angles found by observations surprisingly closely. The misalignment fraction is found to be highly correlated with galaxy morphology both in observations and in the simulation: early-type galaxies are substantially more frequently misaligned than late-type galaxies. The gas fraction is another important factor associated with misalignment in the sense that misalignment increases with decreasing gas fraction. However, there is a significant discrepancy between the SAMI and Horizon-AGN data in the misalignment fraction for the galaxies in dense (cluster) environments. We discuss possible origins of misalignment and disagreement.

**Keywords:** galaxies: kinematics and dynamics — galaxies: evolution — galaxies: interactions — galaxies: structure — galaxies: clusters: general — methods: numerical

### 1. INTRODUCTION

Corresponding author: Sukyoung K. Yi  
 E-mail: [yi@yonsei.ac.kr](mailto:yi@yonsei.ac.kr) (KTS)

Stars and gas, the main constituents of galaxies, are closely linked: gas turns into stars, and stars release gas through mass loss. Since angular momentum is conserved during mass exchange, the rotational axes of stars

and gas in a galaxy are expected to be aligned. However, earlier observations have found that some galaxies have highly misaligned rotations between stars and gas (e.g., Ulrich 1975; Rubin et al. 1992). Moreover, long-slit observations have revealed that galaxies can be misaligned regardless of their mass or morphology (e.g., Bertola et al. 1992; Kuijken et al. 1996; Kannappan & Fabricant 2001; Sweet et al. 2016). Recently, the advent of integral-field spectroscopy (IFS) observations has revealed more detailed kinematic properties of misaligned galaxies (e.g., Sarzi et al. 2006; Coccato et al. 2011, 2015; Davis et al. 2011; Serra et al. 2014; Barrera-Ballesteros et al. 2014, 2015; Krajnović et al. 2015; Katkov et al. 2016; Jin et al. 2016; Bryant et al. 2019). The IFS surveys presented the fraction of misaligned galaxies based on their large samples. For example, Bryant et al. (2019) reported that about 11% of observed galaxies are misaligned, with position angle offsets between the stellar and gas rotational axes being larger than 30 degrees.

There have been many observational and theoretical studies aiming to reveal the origins of star-gas misalignment. Observations suggest that misalignment can be formed if a galaxy accretes gas from a neighboring galaxy or from large-scale filaments in misaligned fashions (e.g., Bertola et al. 1992; Pizzella et al. 2004; Chung et al. 2006; Bureau & Chung 2006). Numerical simulation studies also found hints for origins in the following aspects: (i) galaxy mergers (e.g., Balcells & Quinn 1990; Hernquist & Barnes 1991; Barnes & Hernquist 1996; Bekki 1998; Puerari & Pfenniger 2001; Crocker et al. 2009), (ii) continuous or episodic gas accretions (e.g., Thakar & Ryden 1996; Bournaud & Combes 2003; Brook et al. 2008; Aumer & White 2013; Algorry et al. 2014; van de Voort et al. 2015), and (iii) interactions with nearby galaxies (e.g., De Rijcke et al. 2004). These simulations were based on a small number of galaxies or idealized cases. Considering that misalignment is a highly non-linear phenomenon, we need more comprehensive research based on data with a statistically meaningful size.

Large-volume cosmological simulations offer advantages for studying the star-gas misalignment. Within the simulations, various galaxies with a wide variety of masses, morphologies, and environments evolve in the cosmological context. The large number of galaxies allows us to take a statistical approach. For example, we can investigate how these parameters affect misalignment. Moreover, we can simultaneously observe the past, the present, and the future of misaligned galaxies to identify the sequence of formation and the evolution of misalignment.

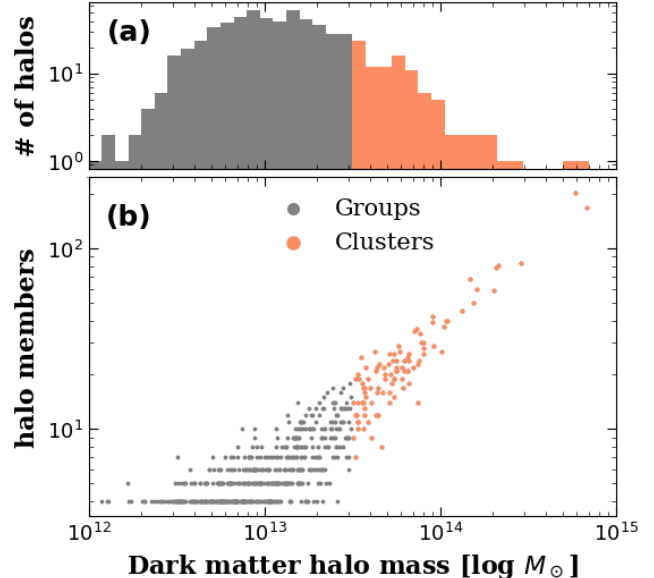


**Figure 1.** The Horizon-AGN galaxy groups (gray) and clusters (orange). A dark matter halo with a mass range of  $10^{12} < M_{\text{vir}}/M_{\odot} < 10^{13.5}$  having more than 4 members is defined as a group. We define halos with dark matter contents above  $10^{13.5} M_{\odot}$  as clusters. Their members are defined when galaxies reside inside 1.5 virial radii ( $R_{200}$ ). There are 500 groups and 102 clusters in Horizon-AGN. Note that Bryant et al. (2019) used 8 clusters which have virial mass heavier than  $10^{14.25} M_{\odot}$ . *Panel (a):* the halo mass histogram of groups and clusters. *Panel (b):* the distribution of the number of member galaxies and the dark matter halo mass.

Starkenburg et al. (2019) recently performed an important investigation of this issue based on the Illustris simulation and found that (i) SMBH feedback and gas stripping during fly-by passages through group environments are the two main channels of misalignment, (ii) several galaxies maintain misaligned components for more than 2 Gyr, and (iii) early-type or gas-poor galaxies have a higher misaligned fractions. Our study confirms some of their key results and presents additional results based on a different simulation, as described in detail in the following sections.

We investigated misaligned galaxies using the large-volume Horizon-AGN simulation (Dubois et al. 2014). Here in this paper (Paper I), we examine the properties of misaligned galaxies using the simulation and compare them with the data from the Sydney-AAO Multi-object Integral field spectrograph (SAMI) Galaxy Survey (Bryant et al. 2015; Croom et al. 2012). In this Paper I, we first try to check how simulations compare with observations in terms of the overall misalignment fraction and the distribution of misalignment angles. Then, we move on to the trend of the misalignment fraction as a function of galaxy morphology, mass, gas fraction, and

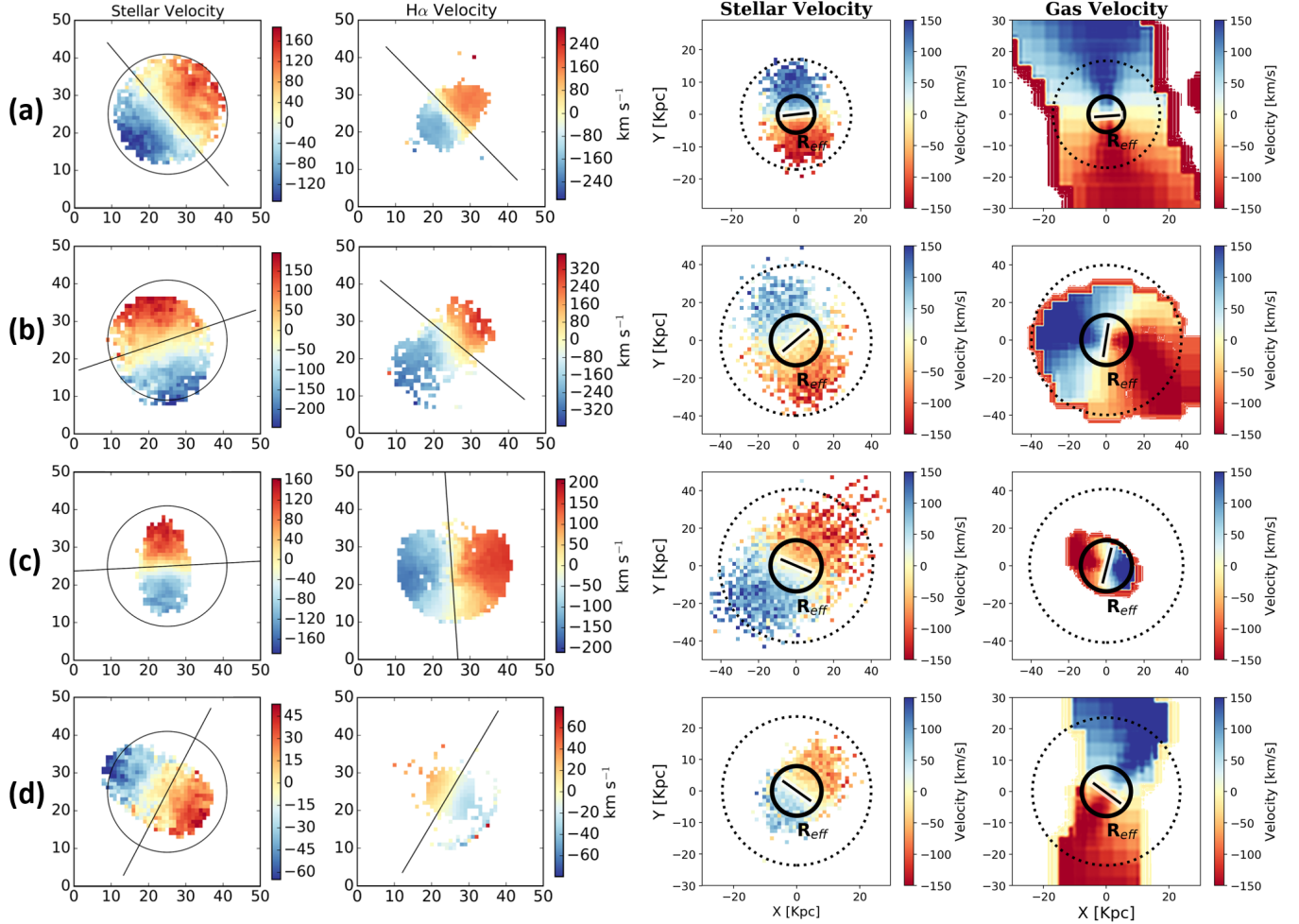


**Figure 2.** Star and gas velocity maps of example galaxies from SAMI (Bryant et al. 2019, the two left columns) and Horizon-AGN (the two right columns). We used “cold gas” instead of ionized gas in the simulation. From top to bottom, four types of galaxies, (a) aligned, (b) misaligned, (c) polar disk (PA offset  $\sim 90^\circ$ ), and (d) counter-rotating galaxies (PA offset  $\sim 180^\circ$ ), are demonstrated. Each rotational axis is expressed by a black line. The circle in the SAMI plot indicates the 15 arcsec size of the SAMI hexabundle. The black circles in the two right columns show  $1 R_{\text{eff}}$  (solid line) and  $3 R_{\text{eff}}$  (dotted line) of the galaxy.

environment. In the following Paper II, we will investigate the formation channels of the misaligned galaxies and quantify the significance of each channel. We will also examine the survival timescale of the star-gas misalignment depending on the properties of the host galaxy. Ultimately, our goal is to identify how gas flows into galaxies and how gas accretion affects galactic evolution.

This paper is organized as follows. In Section 2, we will describe how we select galaxies for SAMI and Horizon-AGN data. In Section 3, we will examine the misaligned galaxies in Horizon-AGN focusing on how the misalignment fraction changes depending on the properties of the galaxies. Also, we will compare the misaligned galaxies in the observations and the simulation. Finally, we will discuss our results in Section 4.

## 2. METHODOLOGY

### 2.1. The Horizon-AGN simulation

Horizon-AGN (Dubois et al. 2014) is one of the state-of-the-art hydrodynamical simulations, run with the AMR code RAMSES (Teyssier 2002), within the cosmological context from the seven-year Wilkinson Microwave Anisotropy Probe results (Komatsu et al. 2011). The side length of the simulation box is 100 Mpc/h, and the maximum (smallest) force resolution is about 1 kpc. The mass resolution is  $8 \times 10^7 M_\odot$  for dark matter, and  $2 \times 10^6 M_\odot$  for stellar particles. Horizon-AGN has 787 snapshots with a time interval of about 17 Myr, but these snapshots have stellar particles only. Sixty-one out of 787 snapshots have full data including stars, gas, dark matter, and sink (black hole) particles. Their

time interval is about 250 Myr. Readers are referred to [Dubois et al. \(2014\)](#) for more details.

## 2.2. Galaxy identification

Galaxies in the simulation were identified using Halo-Maker through the AdaptaHOP algorithm ([Aubert et al. 2004](#)), with the most massive sub-node mode ([Tweed et al. 2009](#)) applied for stellar particles. A minimum of 50 stellar particles, or  $1.7 \times 10^8 M_\odot$ , were used to define a galaxy. In Horizon-AGN, we identified 126,362 galaxies at  $z = 0.055$ . <sup>1</sup>

Galactic models with a small number of stellar particles are not adequate for studying the structure and kinematics of galaxies, as has been discussed in many previous studies. For example, [Dubois et al. \(2016\)](#) classified elliptical galaxies from Horizon-AGN with  $V/\sigma \leq 1$ . They investigated the fraction of elliptical galaxies as a function of galaxy stellar mass and found good agreement with observations when  $M_* \gtrsim 2 \times 10^{10} M_\odot$ . Similar exercises and conclusions have been made based on other simulations ([Snyder et al. 2015](#); [Rodriguez-Gomez et al. 2017](#); [Penoyre et al. 2017](#)). Therefore, we limit our study to galaxies with stellar mass above  $10^{10} M_\odot$  which corresponds to  $\sim 3,000$  stellar particles. In the case of Horizon-AGN, the number of galaxies with stellar mass above  $10^{10} M_\odot$  is 27,908 out of 126,362 at  $z = 0.055$ .

We use kinematic classification of morphology. Higher  $V/\sigma$  galaxies tend to have disk-shape structures due to the highly aligned motion of stars, while lower  $V/\sigma$  galaxies tend to have spheroidal shape structures. The galaxies are classified into early-type galaxies (ETGs) and late-type galaxies (LTGs) using a  $V/\sigma$  cut of 1 (see, [Dubois et al. 2016](#)). It should be noted that  $V/\sigma$  can be measured to be different when measured kinematically (as was the case in [Dubois et al. 2016](#)) and through IFS after mock imaging for the same galaxies ([van de Sande et al. 2019](#)).

## 2.3. Cluster and group identification

We identified groups and clusters in Horizon-AGN as follows. We first identified dark matter halos with  $M_{\text{vir}} > 10^{11} M_\odot$  and counted their member galaxies with  $M_* > 10^{10} M_\odot$  within 1.5 virial radii ( $R_{200}$ ). A halo is classified as a “group” when its mass is in the range of  $10^{12} < M_{\text{vir}}/M_\odot < 10^{13.5}$  and its member galaxies number at least 4. Clusters are defined as having greater mass than that ( $M_{\text{vir}}/M_\odot > 10^{13.5}$ ). Thus, Horizon-AGN is found to contain 500 groups and 102 clusters

at  $z=0.055$ . Fig. 1-(a) shows the histogram of Horizon-AGN groups (gray) and clusters (orange). We note that Horizon-AGN and typical volume simulations with 100 Mpc side-length (e.g., Illustris, Eagle, and so on) would not have so many massive clusters as in the observation. Also, the mass range of the Horizon-AGN clusters is intentionally kept broad so that we can investigate the possible presence of cluster (halo) mass dependence on the misalignment. Fig. 1-(b) shows the number of member galaxies against the group mass. The total numbers of member galaxies are 5,924 and 2,711 inside groups and clusters, respectively.

## 2.4. Galactic gas and the rotational axis

Since we are interested in the gas properties of individual galaxies, we divide the gas in the simulation into galactic cold gas and (non-cold) “surroundings” as follows. We use a linear cut in the logarithmic density-temperature plane using Equation (1) from [Torrey et al. \(2012\)](#):

$$\log(T/[K]) = 6 + 0.25 \log(\rho/10^{10} [M_\odot h^2 \text{kpc}^{-3}]). \quad (1)$$

“Galactic cold gas”, the low-temperature side, is used for star formation in the simulation. According to this scheme, it has a temperature of roughly 10,000-30,000 K depending on the density. The cold gas is located at the central and disk parts of the galaxy and found to represent the kinematic property of the interstellar medium. Also, the motion of the cold gas will correspond to the observed gas motion, because IFS observations such as SAMI measured gas motion using  $\text{H}\alpha$  emission lines ( $\sim 10,000$  K). “The surrounding gas”, on the other hand, is the gas above the density-temperature criterion. It corresponds to intracluster medium or intergalactic medium. To investigate the rotation of gas in the galaxies, we focus only upon the cold gas. Note that the Horizon-AGN simulation cannot resolve molecular gas, which has an extremely cold temperature.

To measure the rotational axes of a galaxy, we measure the velocity of all stellar particles and gas cells belonging to the galaxy. We measure their angular momentum with their position and velocity relative to the galactic center. We define the rotational axes of the galaxy in terms of the direction of the net angular momentum of each component. We measure the rotational axes inside one effective radius ( $R_{\text{eff}}$ ), encompassing half of the total stellar mass (half projected stellar mass). We measured the position angle (PA) offset between the rotational axes of the stars and gas. The PA offset (misaligned angle) is defined to be within the range of 0 (aligned) to 180 degrees (counter-rotating).

We draw stellar and gas velocity maps similar to IFS data using Horizon-AGN galaxies. Some examples are

<sup>1</sup> We considered the 761st snapshot ( $z = 0.055$ ) rather than the last snapshot at  $z = 0$ , for comparison with the observation in this study, mainly because the observed galaxies used in this study are at that distance as well.

shown in Fig. 2, with the observational data from SAMI (Bryant et al. 2019) for comparison. The effective radius is marked with a black solid circle, and each rotation axis is shown with a black line. The simulation has reproduced many different types of misaligned galaxies, including polar disk galaxies (PA offset  $\sim 90^\circ$ ) and counter-rotating galaxies (PA offset  $\sim 180^\circ$ ).

### 3. RESULT

#### 3.1. Comparing with the SAMI data

##### 3.1.1. SAMI samples

Bryant et al. (2019) used the SAMI sample for which PAs are measured for both gas and stars: 486 out of 833 galaxies in the field/group regions and 136 out of 380 in cluster regions. They measured the PA offset from the difference between the two PAs (stars and gas). According to Bryant et al. (2019), the error of the fitted PAs is estimated to be  $\pm 10$  degrees and to be much larger for galaxies with a low gas content or with low signal-to-noise-ratio spectrum. They classified galaxies as “misaligned” when they had a PA offset larger than 30 degrees for direct comparison to the previous papers (e.g., Lagos et al. 2015; Davis & Bureau 2016). In this paper, we also used their criterion of star-gas misalignment to compare our results.

SAMI classified the morphology of galaxies by visual inspection. The detailed method can be found in Cortese et al. (2016). The masses of the field/group galaxies range from  $10^8 M_\odot$  to  $5 \times 10^{11} M_\odot$ , while those of the cluster sample range  $10^{10} M_\odot$  through  $5 \times 10^{12} M_\odot$ . We would like to remind the readers that the lower mass limit of our Horizon-AGN galaxies is  $10^{10} M_\odot$ . The virial masses of the SAMI clusters are  $10^{14.25} < M_{200}/M_\odot < 10^{15.19}$  (Owers et al. 2017), which is much greater than those of the Horizon-AGN clusters shown in Fig. 1. We will discuss the impact of this difference in Section 4.1. The redshift range of the SAMI data is up to 0.1, but its cluster galaxies have a narrower redshift range ( $0.02 < z < 0.07$ ). The detailed description of the SAMI cluster can be found in Owers et al. (2017).

##### 3.1.2. Gas detection limit

The SAMI misalignment study (Bryant et al. 2019) used only the galaxies whose PAs have been measured for both gas and stars. A considerable number of observed galaxies were excluded due to the low gas emission flux. Therefore, it is necessary to set a detection limit for gas kinematics in the simulation that is consistent with observations.

The SAMI study (Bryant et al. 2019) does not have comparable measures of the gas contents or gas fractions of its galaxies. Thus, we determine the gas de-

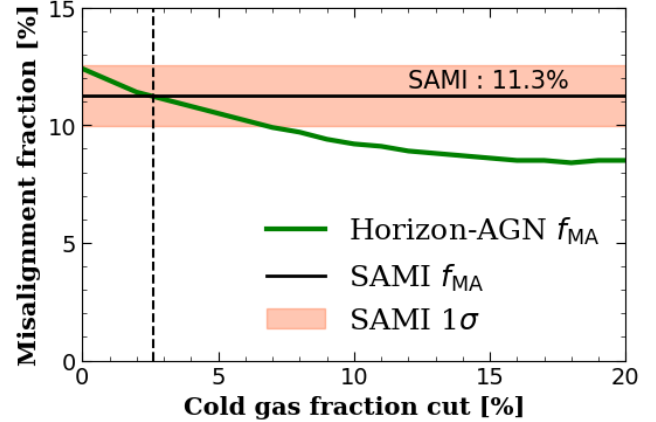


**Figure 3.** The Horizon-AGN misalignment fraction depending on the cold gas fraction cut. We regard the cold gas fraction criterion as a gas detection limit. We measure the misalignment fraction (green line) of “observable galaxies” which are above a certain gas fraction. While they show a monotonic, negative trend, Horizon-AGN galaxies with  $f_{\text{gas}} \gtrsim 0.03$  (vertical dotted line) reproduce the SAMI misalignment fraction of 11.3% (horizontal line). Note that the misalignment fraction in the simulation is not very sensitive to the gas fraction cut. The binomial  $1\sigma$  error of the SAMI sample is expressed in the shaded area.

tection limit indirectly from the misalignment fraction, which depends upon the cold gas fraction. We define the gas fraction as the mass ratio of cold gas to stars ( $M_{\text{cold gas}}/M_*$ ) within  $1 R_{\text{eff}}$  of the galaxy. After that, we regard the gas fraction as a gas detection limit; relatively gas-rich galaxies are considered “observable”. Fig. 3 shows a monotonic, negative trend between the misalignment fraction and the gas fraction cut. The Horizon-AGN galaxies with  $f_{\text{gas}} > 0.03$  reproduce the SAMI misalignment fraction of 11.3%, which is the fraction of galaxies with a PA offset exceeding 30 degrees. We therefore conclude that the gas detection limit roughly corresponds to a gas fraction of 3% within  $1 R_{\text{eff}}$ . With this criterion, the total number of “observable” galaxies is 26,330 at  $z = 0.055$ . Although this is an arbitrary value, we want to note that the misalignment fraction in the simulation is not very sensitive to gas fraction according to Fig. 3.

##### 3.1.3. The distribution of the star-gas PA offset

Observational data are projected to the perpendicular plane to the line-of-sight. In order to minimize bias from the projection effect, we have performed a Monte-Carlo simulation of projection as many as 1,000 times on each model galaxy and measured their PA offsets.

The histogram of star-gas PA offset is shown in Fig. 4. Panel (a) shows the histograms of the 622 galaxies from SAMI (red) and the 26,330 (times 1,000 projec-

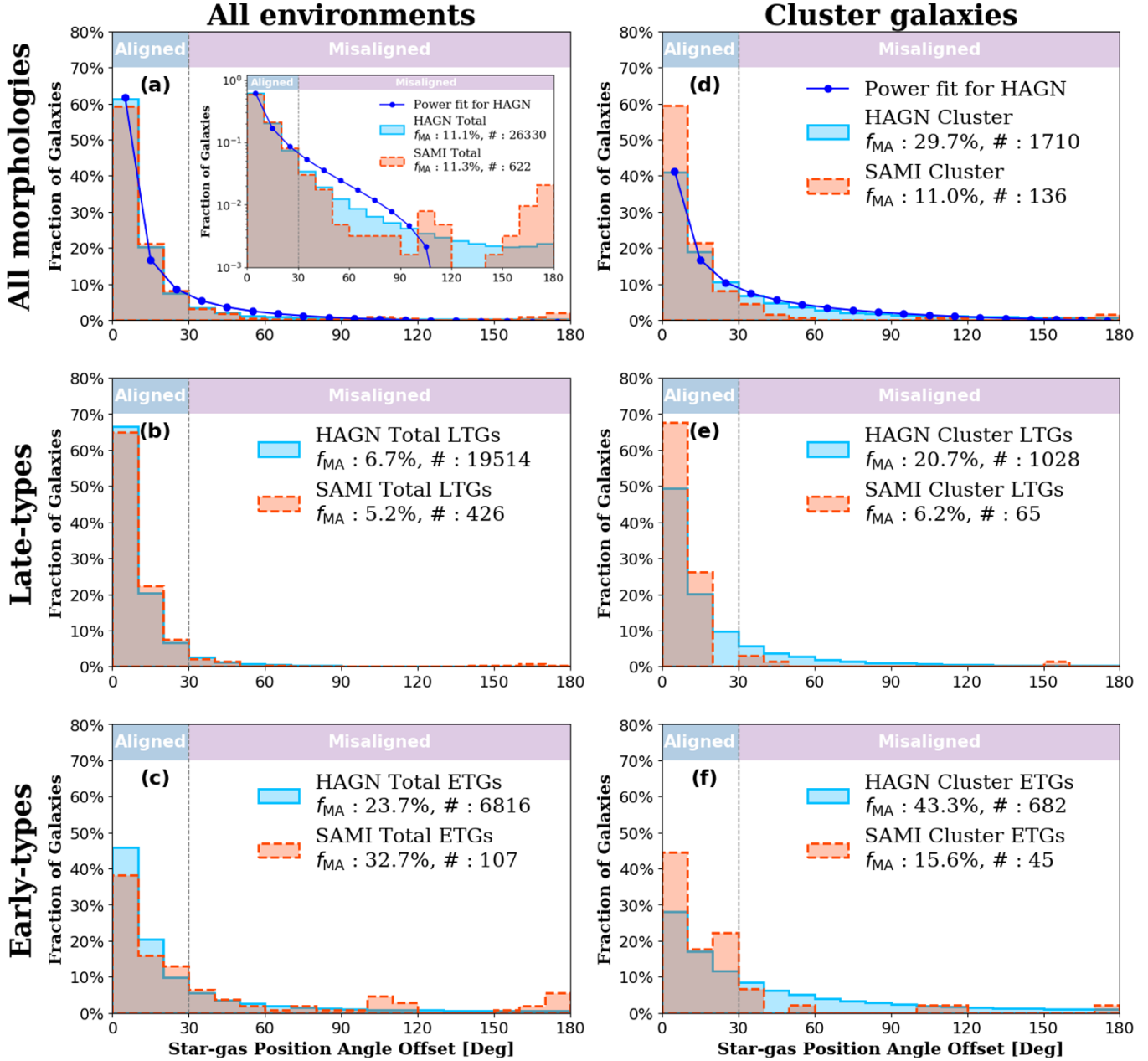


**Figure 4.** The distribution of star-gas PA offset in Horizon-AGN (blue) and SAMI (red) galaxies. We have performed a Monte-Carlo simulation of projection on the Horizon-AGN galaxies as many as 1,000 times to minimize bias from the projection effect. We classified misaligned galaxies when their PA offset exceeds 30 degrees, following previous researches (e.g., Bryant et al. 2019). The legend shows the misalignment fractions and number of samples. The left column shows all galaxies, regardless of their environment, while the right column shows galaxies belonging to clusters. *Top panels*: the galaxies from Horizon-AGN and SAMI, regardless of their morphological classification. The best-fit power-law for the Horizon-AGN distribution is expressed as the blue curve. For Panel (a), the inset diagram presents the same histogram in a logarithmic scale to highlight the apparent 90- and 180-degree peaks. *Middle panels*: the distribution of late-type galaxies ( $V/\sigma > 1$ ). *Bottom panels*: the distribution of early-type galaxies ( $V/\sigma \leq 1$ ).

tions) galaxies from Horizon-AGN (green). [Bryant et al. \(2019\)](#) reported that about  $11.3 \pm 1.2\%$  of galaxies are misaligned (PA offset  $> 30^\circ$ ), and Horizon-AGN galaxies with  $f_{\text{gas}} > 0.03$  show a misalignment fraction of  $11.1 \pm 0.1\%$ .

The Horizon-AGN galaxies show a remarkably similar distribution to that of the SAMI galaxies. The best-fit power-law indices are  $-1.254$  for SAMI and  $-1.284$  for the Horizon-AGN data. We present for visual guidance the power-law fits (in blue curves) to the Horizon-AGN data in Fig. 4-(a). We evaluate the likelihood that the two distributions are drawn from the same population, using a two-sample Kolmogorov-Smirnov (KS) test. The KS-test statistic is  $0.034$  and the p-value is  $0.454$ , which suggests that they are likely to be drawn from the same population. The PA offset distribution is a steeply decaying function with respect to PA offset. This implies that once the PA misalignment is set, it decays gradually with time, no matter what the physical mechanisms may be.

We also present the same histogram with a logarithmic scale in the inset diagram to highlight the apparent two peaks at high PA offsets. Prominent differences between the SAMI and Horizon-AGN data appear around  $90$  and  $180$  degrees. [Bryant et al. \(2019\)](#) suggested that those peaks are linked with the dynamical settling-down processes of PA offsets. The star-gas misalignments at  $90$  and  $180$  degrees may be more stable than at other angles because the integrated torque between the stellar and gas disks can be more easily cancelled at these two angles. Similar peaks were found in the ATLAS 3D dataset ([Davis & Bureau 2016](#)). Also, the polar disk structures of S0 galaxies (e.g., [Schweizer et al. 1983](#); [van Gorkom et al. 1987](#); [Whitmore et al. 1990](#)) imply the presence of a  $90$ -degree peak. Horizon-AGN, however, does not reproduce the  $90$ - and  $180$ -degree peaks. This might be due to the insufficient spatial resolution of the simulation, and the stability of the two peaks may depend on how accurately thin disks are realized in the simulation. Horizon-AGN has a maximum (best) spatial resolution of roughly  $1$  kpc, and with this it is difficult to resolve/reproduce a thin disk. Therefore, in Horizon-AGN, galactic gas disks are not as thin as in real galaxies. The outer parts of the apparently-thick disk will start to feel an imbalance in torque from competing directions (i.e., from the stellar disk). As a result, misalignments of around  $90$  degree for example may decay more easily when resolution is insufficient.

#### 3.1.4. Morphology and the misalignment

The star-gas PA offset distributions of LTGs and ETGs are shown in Figs. 4-(b) and -(c), respectively.

LTGs tend to be more aligned than ETGs in both the observation and the simulation. For a reference, [Starkenburg et al. \(2019\)](#) found a consistent result regarding the morphology dependence of the misalignment fraction. The misalignment fractions of LTGs are comparable between SAMI ( $5.2 \pm 0.7\%$ ) and Horizon-AGN ( $6.7 \pm 0.1\%$ ). The shape of the histograms are also consistent between them: the best-fit power-law indices are  $-1.323$  for SAMI and  $-1.254$  for the Horizon-AGN data. (KS-test statistic =  $0.034$ , and p-value =  $0.691$ ). On the other hand, the misalignment fractions of ETGs are substantially different between the two samples:  $32.7 \pm 6.6\%$  (SAMI) and  $23.7 \pm 0.2\%$  (Horizon-AGN). The overall distribution of the PA offset too is markedly different: the best-fit power-law indices are  $-0.931$  for SAMI and  $-1.035$  for Horizon-AGN data (KS-test statistic =  $0.130$ , and p-value =  $0.050$ ).

The discrepancy between the results from SAMI and Horizon-AGN may come from multiple origins. One may be due to the different classification methods applied. The Horizon-AGN galaxies are classified as ETGs and LTGs using the cut of  $V/\sigma = 1$ , while the SAMI galaxies are classified via visual inspection. For example, a good fraction of S0 galaxies classified as ETGs by visual inspection may be classified as LTGs by the  $V/\sigma$  criterion. If we change the morphology criterion to  $V/\sigma = 0.8$ , the misalignment fraction in Horizon-AGN becomes  $29.5 \pm 0.3\%$  and the best fit power-law index becomes  $-0.953$  (KS-test statistic =  $0.078$ , and p-value =  $0.485$ ).

#### 3.1.5. Cluster environment and misalignment

The star-gas PA offset distribution and misalignment fraction of cluster galaxies are shown in Fig. 4-(d). Since only a small fraction of Horizon-AGN galaxies belong to the cluster environment ( $\sim 10\%$ , or less), the histograms of group/field galaxies would be nearly the same as those of all galaxies (the left panels). In the case of Horizon-AGN, we find that cluster galaxies have a misalignment fraction  $2.7$  times higher ( $29.7 \pm 0.5\%$ ) than the group-/field galaxies ( $11.1 \pm 0.1\%$ ). This result significantly disagrees with the SAMI galaxies that show no clear difference is apparent between cluster and non-cluster samples. The best fit power-law indices are  $-1.249$  for SAMI and  $-0.954$  for Horizon-AGN data (KS-test statistic =  $0.236$ , and p-value =  $3.710\text{e-}7$ ).

We note in Figs. 4-(b) and (c) that the misalignment fraction is higher for ETGs. Thus, since ETGs are more frequently found in dense environments ([Dressler 1980](#)), the misalignment fraction is also expected to be higher in denser environments. In this sense, part of the higher misalignment fraction of cluster galaxies in Horizon-AGN can be understood. However, this is not

the whole story when we divide the cluster galaxies into LTGs (Fig. 4-(e)), and ETGs (Fig. 4-(f)). The misalignment fraction of the cluster galaxies in Horizon-AGN (29.7%) is even higher than that of the general ETGs (23.7%), meaning that even if clusters are entirely made up of ETGs, their misalignment fractions cannot be explained by the morphology mix alone.

We also found higher misalignment fractions in cluster environments in the Horizon-AGN simulation, regardless of the morphologies of galaxies (LTG:  $20.7 \pm 0.5\%$ , ETG:  $43.3 \pm 0.9\%$ ) by a factor of 3.1 (LTG) and 1.8 (ETG) compared to the whole sample (LTG: 6.7%, ETG: 23.7%). Thus, something other than just the morphology mix is affecting the misalignment of cluster galaxies, perhaps through some environmental effects (see Section 4.1.). Bryant et al. (2019) however reported in their SAMI observations that the misalignment fraction of LTGs is increased in the cluster environment whereas the misalignment fraction of ETGs is greatly reduced. While the former is consistent with Horizon-AGN, the latter is not. Meanwhile, both the misalignment fractions and distributions are quite different. The best-fit power-law indices of LTGs are  $-1.365$  and  $-1.085$  for SAMI and Horizon-AGN, respectively (KS-test statistic = 0.248, and p-value = 5.271e-4). The two ETG samples also have different PA offset distributions. The best fit power-law indices are  $-0.984$  and  $-0.736$  for SAMI and Horizon-AGN, respectively (KS-test statistic = 0.302, and p-value = 3.908e-4). At this stage, we find it difficult to understand the origin of this discrepancy: it could potentially come from the differences in gas measurement methods. We will discuss this phenomenon and the reasons behind it further in Section 4.1.

### 3.2. Properties of Horizon-AGN misaligned galaxies

In this section, we explore the properties of misaligned galaxies, hoping to pin down the main drivers of star-gas misalignment. Fig. 5 shows the star-gas PA offsets of Horizon-AGN galaxies depending on their properties (i.e., stellar mass, gas mass, gas fraction, and  $V/\sigma$  ratio). Each point is a Horizon-AGN galaxy color-coded based on the star-gas PA offset. The size of each point scales with the PA offset. Meanwhile, Fig. 6 is a 2D histogram showing the misalignment fraction, which is the fraction of galaxies with a PA offset exceeding 30 degrees, on the same planes of Fig. 5. In the case of Fig. 6, the 0.5 and  $1\sigma$  contours are presented. Each pixel contains at least 5 galaxies to ensure statistical significance.

In these two figures, we used all of the Horizon-AGN galaxies with  $M_* > 2 \times 10^8 M_\odot$ , including relatively low-mass galaxies to examine the mass resolution problem,

except in the case of Panels (d) of the two figures. The shaded areas show the low-mass region ( $M_* < 10^{10} M_\odot$ ). As we mentioned above (See Section 2.2), low-mass galaxies exhibit large values of PA offsets. This is likely a result of the fact that the current mass resolution allows only a small number of star particles and gas cells for low-mass galaxies, making it difficult to generate a realistic disk structure in which case PA alignment is difficult to achieve. Our mass cut of  $M_* > 10^{10} M_\odot$  (discussed in Section 2.2) is therefore justified by this argument. Panels (d) of the two figures hence show the Horizon-AGN galaxies above  $10^{10} M_\odot$ .

#### 3.2.1. Galaxy kinematic morphology

One remarkable result is a strong correlation between star-gas misalignment and galaxy morphology, as shown in Figs. 5-(a) and 6-(a). Galaxies with lower  $V/\sigma$  ratios tend to be more misaligned, in agreement with observations. In the figures, the morphology criterion ( $V/\sigma = 1$ ) is expressed as a black dashed line. Note that extremely slow-rotating galaxies ( $V/\sigma < 0.1$ ) must be treated with care. These galaxies are dispersion-dominated systems and their stellar rotational axis is not well defined. Excluding the galaxies with  $V/\sigma < 0.1$  does not affect our result much.

Higher  $V/\sigma$  galaxies, or LTGs, have rotation-dominated stellar component and usually have lots of gas. These properties may be linked with the misalignment fraction. In this subsection, we will focus on the kinematic morphology first. The effect of the gas content will be covered in the next subsection.

The dynamical settling time in relation to the ellipticity ( $\epsilon = 1 - C/A$ , where A and C are intrinsic major and minor axes, respectively) of galaxies may explain part of the different misalignment fractions between LTGs and ETGs. Fast-rotators tend to have higher ellipticities than slow-rotators (e.g., the spin-ellipticity distribution. Emsellem et al. 2007). Bryant et al. (2019) suggested that the shape of the stellar mass distribution affects the dynamical settling time (or decaying time) of the PA offset, which is the time needed for the PA offset to become aligned or counter-rotating. The rotating gas disk should be affected by gravitational torque from the stellar mass distribution and gradually become aligned with the stellar disk. Bryant et al. (2019) presented the settling time as:

$$t_s \propto \frac{R}{V_{\text{rot}}(2\epsilon - \epsilon^2)|\cos(\phi)|}, \quad (2)$$

where  $V_{\text{rot}}$  is the rotational velocity of a gas disk,  $R$  is the radius of the disk, and  $\phi$  is the inclination angle between the two disks (See also Davis & Bureau 2016).

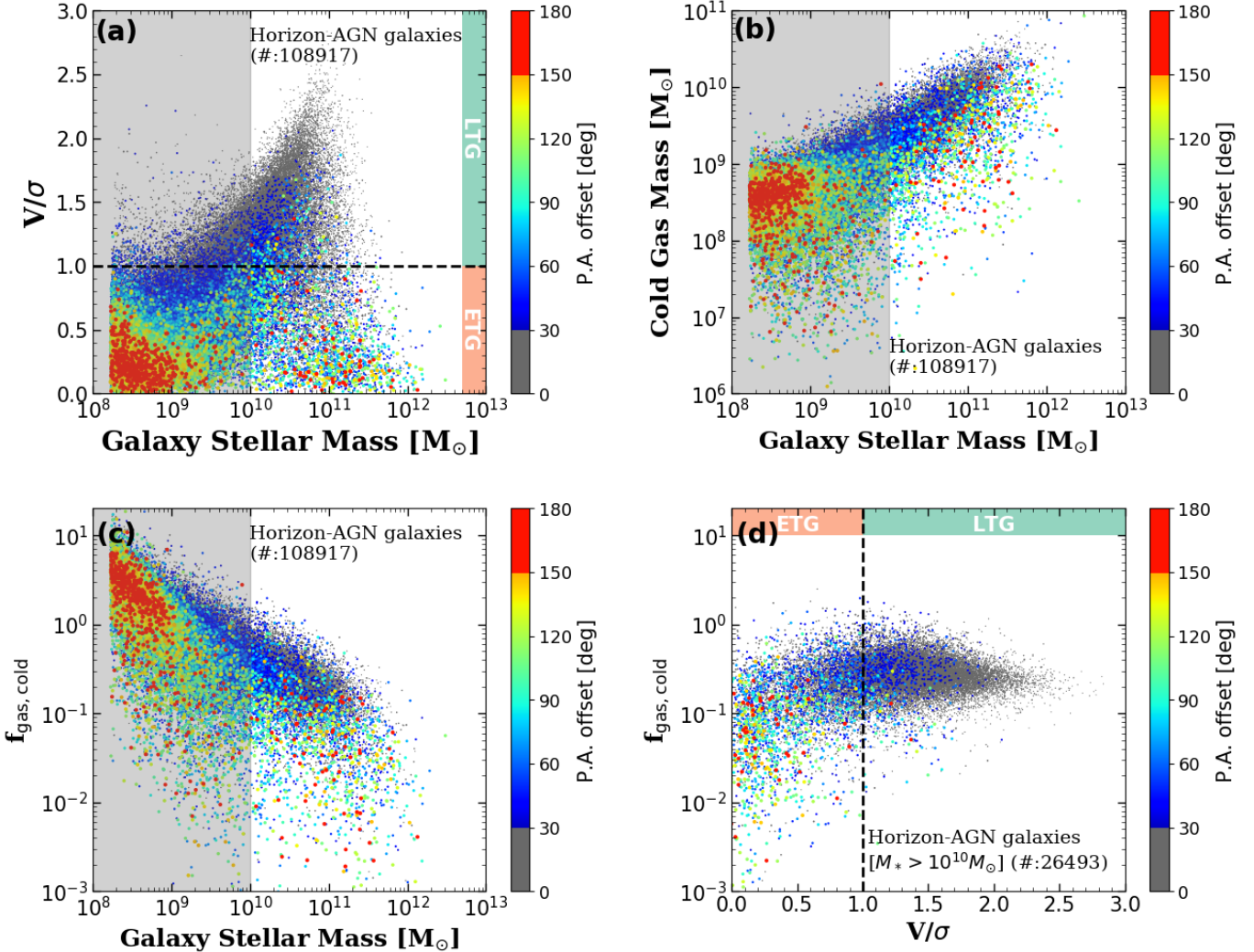


**Figure 5.** The distribution of the star-gas PA offset depending on the properties (stellar mass, cold gas mass, cold gas fraction and  $V/\sigma$ ) of Horizon-AGN galaxies. We define the gas fraction as the mass ratio of cold gas to stars ( $M_{\text{cold gas}}/M_*$ ) within  $1 R_{\text{eff}}$  of the galaxy. All points in the panels are color-coded based on the PA offset. Low-mass ( $M_* < 10^{10} M_\odot$ ) galaxies in the gray shaded regions in panels (a), (b), and (c) have been excluded from the analysis. Panel (d) shows only the galaxies with stellar masses above  $10^{10} M_\odot$ . Each point-size scales with PA offset to highlight misaligned galaxies. Gas fraction and gas mass are measured inside  $1 R_{\text{eff}}$ . The black dashed line ( $V/\sigma = 1$ ) divides galaxies into LTGs and ETGs. Overall, lower  $V/\sigma$  and gas-poor galaxies are more likely to be misaligned.

Equation (2) states that the settling time increases with ellipticity and misalignment angle.

Based on this equation, Bryant et al. (2019) suggested that the intrinsic ellipticity alone makes the settling-timescale for ETGs 2.7 times larger than that for LTGs. This estimate assumes that there is no morphological dependence on  $R/V_{\text{rot}}$  and that the ellipticities of ETGs and LTGs are 0.2 and 0.8, respectively. Since the difference in the misalignment fraction between ETGs and LTGs is about 6.3 times in the SAMI sample, they concluded that the effect of ellipticity on dynamical settling time alone (i.e., Equation (2)) is insufficient to explain the difference in misalignment fraction. Mean-

while, Horizon-AGN presents a factor of 3.6 between ETGs and LTGs. Again, this difference is too high to be driven by the ellipticity in dynamical settling time (2.7 times) alone.

### 3.2.2. The gas contents

Misalignment is strongly affected by the gas contents of galaxies, as shown in Figs. 5-(b), (c) and 6-(b), (c). Overall, the galaxies containing a smaller amount of gas more often show star-gas misalignment. While the gas fraction and  $V/\sigma$  (morphology) are closely related, we find that they independently affect the misalignment fraction, as shown in Fig. 6-(d). The smaller the two parameters are, the higher the misalignment fraction is.

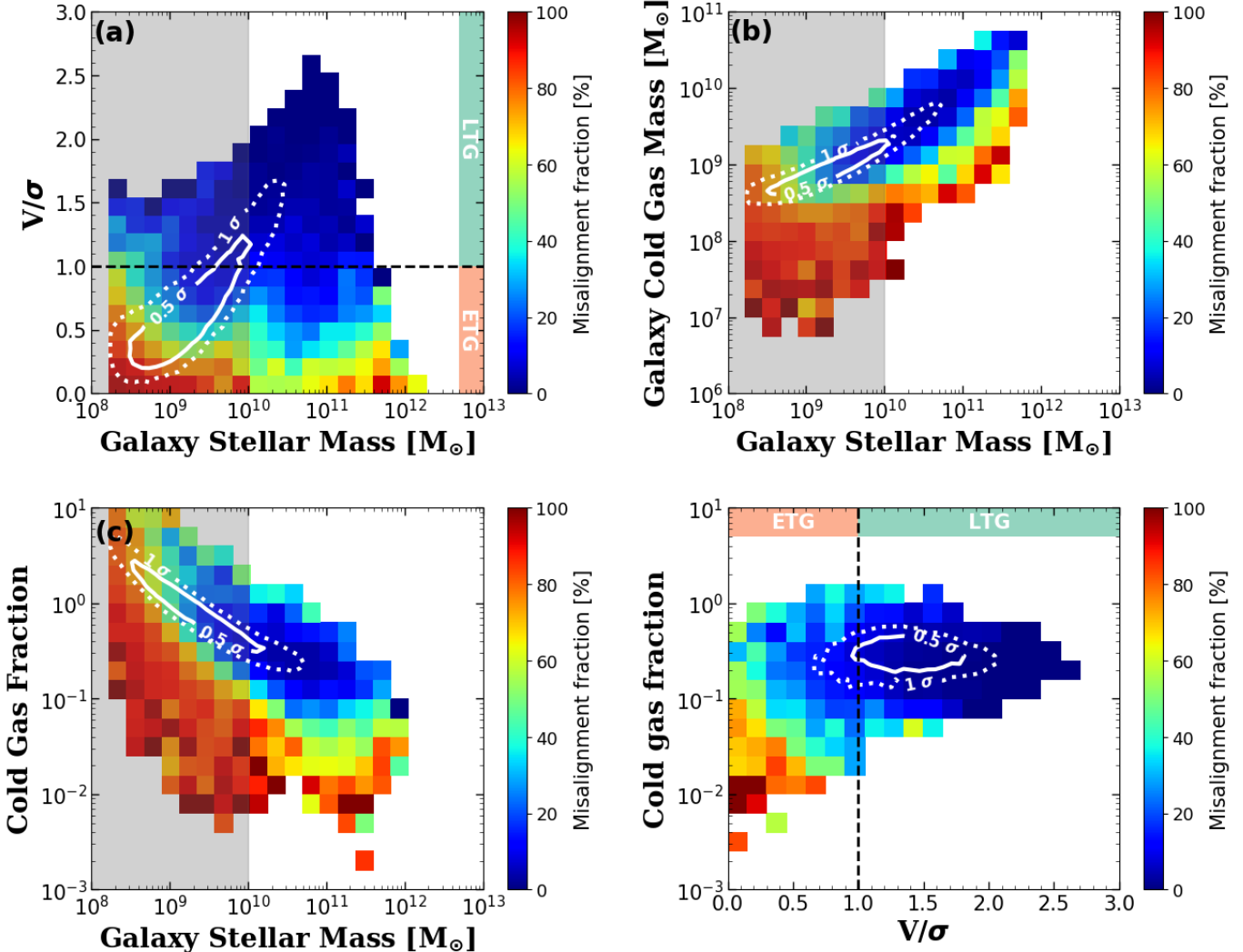


**Figure 6.** 2D histogram showing the star-gas misalignment fraction depending on the properties of Horizon-AGN galaxies based on Fig. 5. We classified misaligned galaxies when their PA offset exceeds 30 degrees. The white contours show the  $0.5\sigma$  (solid line) and  $1\sigma$  (dotted line) distributions of galaxies. Each pixel contains at least 5 galaxies.

We first focus on the impact of the amount of gas. Galaxies maintain their gas kinematic properties (e.g., direction and magnitude of spin) better when richer in gas. For example, the gas kinematic properties of a galaxy are influenced by gas accretion, but if the galaxy is already gas-rich, the impact of external gas accretion would naturally be small. Considering this effect alone, PA offset due to external gas accretion is expected to be smaller when a galaxy is richer in gas.

While the gas mass can partially explain the trend, we also find that the formation of misalignment is linked with gas loss (e.g., gas stripping due to the group/cluster environments). We will discuss the gas stripping in Section 4.1, and the origin of the misalignment in the follow-up paper.

The interaction between stellar and gas disks also affects the PA offset. While the settling-timescale shown in Equation (2) deals with the torque on the gas disk by the stellar mass distribution, a massive gas disk also attracts the stellar disk and reduces the time for gas and stars to be aligned. Considering this, the more massive the gaseous disk (or the higher the gas fraction), the quicker the PA offset decay.

Finally, star formation in the gas disk may make the gas and stellar disks appear gradually more aligned as new stars born with the kinematic characteristics of the gas disk are added to the existing stars, affecting the mean properties of the stellar distribution.

### 3.2.3. Galaxy mass

One of the important factors governing the properties of a galaxy is its mass. Therefore, the misalignment

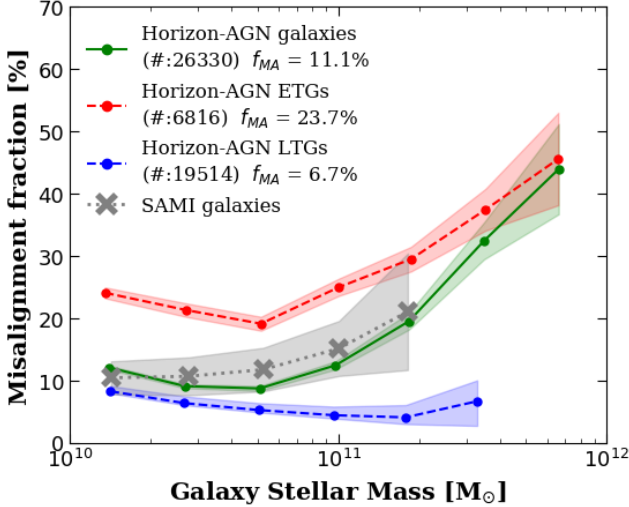


**Figure 7.** The misalignment fraction of Horizon-AGN galaxies as functions of galaxy stellar mass. The gray dotted line is the misalignment fraction measured by [Bryant et al. \(2019\)](#). The misalignment fractions for all Horizon-AGN galaxies (green), for ETGs (red), and for LTGs (blue) as functions of stellar mass are shown in the figure. Each point contains at least 10 galaxies, and shadowed regions show the  $1\sigma$  error of the mean of a binomial distribution. The whole sample (green line) shows that more massive galaxies have higher misalignment fractions, which appears to originate from the mass-morphology relation. While the misalignment fraction of LTGs (blue) remains almost constant, massive ETGs are found to have an enhanced misalignment fraction, since they tend to have relatively low gas fraction and low  $V/\sigma$  ratio.

may be affected by the masses of galaxies. Fig. 6-(a) shows that more massive galaxies show higher values of misalignment fractions, which is largely due to the fact that more massive galaxies tend to be earlier in type ( $V/\sigma \leq 1$ ). In order to clarify the effect of stellar mass upon the misalignment fraction, we present Fig. 7 here. The green line shows the misalignment fraction of the Horizon-AGN galaxy sample. For comparison, we plot the SAMI misalignment fractions as a gray dotted line. The more massive galaxies have higher misalignment fractions. We divide the galaxies into ETGs (red) and LTGs (blue) to ensure that the mass trend comes from morphology. In the low-mass region  $M_* < 10^{11}$ , the green line is located near the blue line, since LTGs numerically overwhelm ETGs. On the other hand, the green line follows the red line in the relatively high-mass region. Therefore, the mass trend comes from a combination of massive galaxies being more likely to be ETGs (e.g., [Conselice 2006](#); [Ilbert et al. 2010](#); [Bundy et al. 2010](#)), and ETGs showing misalignment more often. Note that massive ETGs are found to have an en-

hanced misalignment fraction, since they tend to have both a relatively low gas fraction and  $V/\sigma$  ratio.

[Bryant et al. \(2019\)](#) also found this mass trend (gray line) and came to the same conclusion. They reported that massive galaxies have a slightly higher misalignment fraction than low-mass galaxies, but that the effect of morphology dominates over that of stellar mass.

### 3.3. Group & cluster environment effect

Groups and clusters are gravitationally bound structures with many galaxies. The properties of galaxies in dense areas are affected by their environments, including factors such as the morphology-density relation ([Dressler 1980](#)), star formation quenching ([Gómez et al. 2003](#)), and gas stripping ([Gunn & Gott 1972](#); [Quilis et al. 2000](#)).

Star-gas misalignment in Horizon-AGN shows a clear trend with not only the morphology of galaxies, but also with the environment. This was already visible in Fig. 4: the cluster galaxies in Panel (d) had more than a factor-of-two-higher value of misalignment fraction compared to the whole sample (which is dominated by field galaxies). Figs. 8-(a) and -(b) further demonstrate that group and cluster halos with greater masses or more members have higher values of misalignment fraction. While [Bryant et al. \(2019\)](#) found that halo mass had no effect upon misalignment fraction in the SAMI data, Horizon-AGN galaxies show a strong environmental trend. Figs. 8-(c) and -(d) imply that the enhanced misalignment fraction in clusters is linked with the low gas fraction of the member galaxies, which might be related with the gas stripping process in cluster environments. This issue will be discussed further in Section 4.1.

## 4. DISCUSSION

### 4.1. The environmental effect

A significant difference between SAMI and Horizon-AGN was found in dense environments. Section 3.1.5 showed that Horizon-AGN has enhanced misalignment fractions in cluster environments, regardless of the galactic morphology. Also, the misalignment fraction is strongly linked with the halo mass or the number of its members (Section 3.3). On the other hand, SAMI, as well as ATLAS 3D ([Davis et al. 2011](#)) and MaNGA ([Jin et al. 2016](#)), show a different trend. The cause of this discrepancy must be examined to understand the star-gas misalignment properly.

#### 4.1.1. Ram pressure

The gas of cluster galaxies can be influenced by interactions with the ICM of the cluster (e.g., [Gunn & Gott](#)

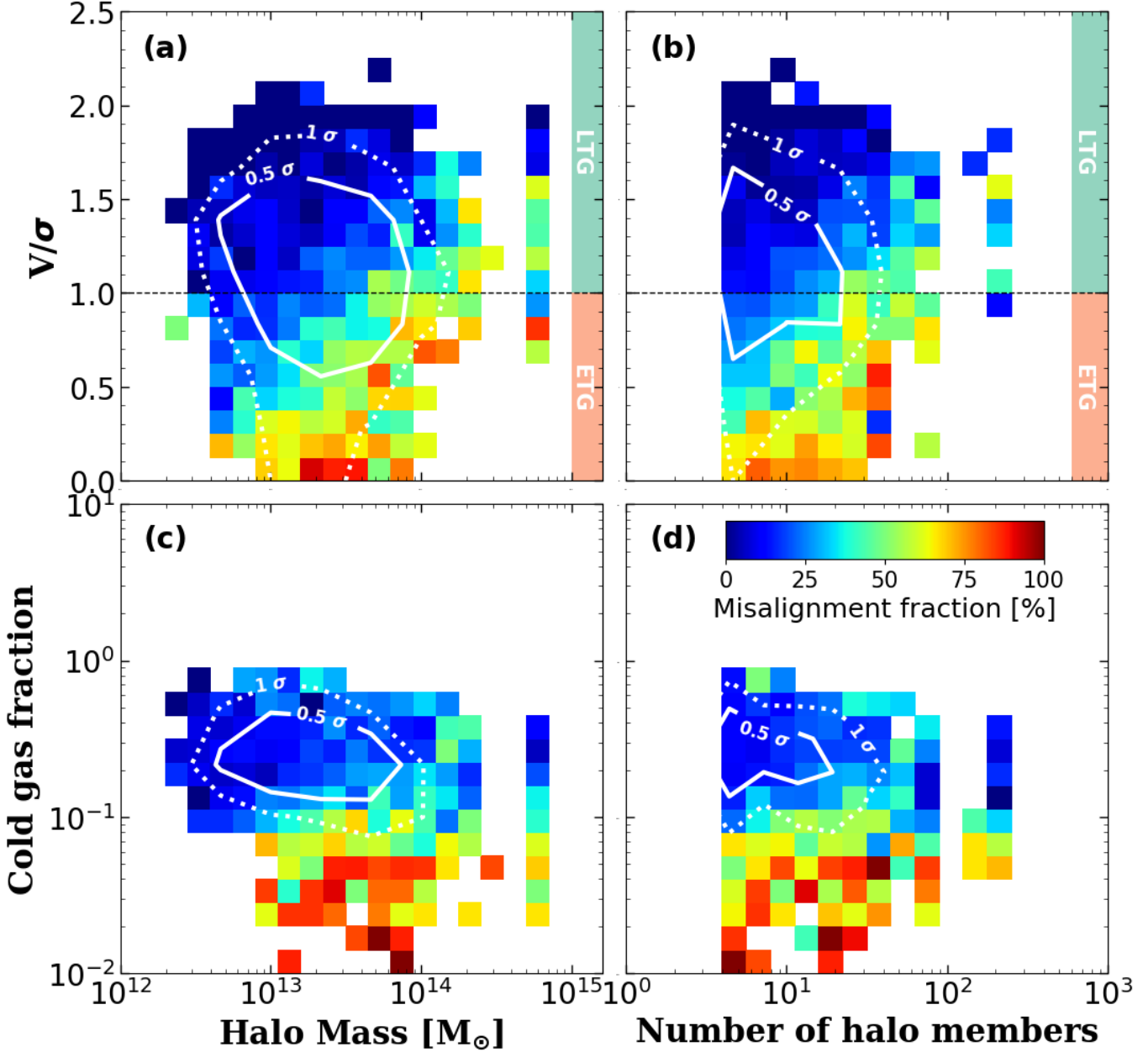


**Figure 8.** 2D histogram showing the misalignment fraction (PA offset  $> 30^\circ$ ) depending on the group environment of Horizon-AGN galaxies. Each pixel contains at least 5 galaxies. Group and cluster halos with greater masses or members have higher misalignment fraction values. *Panel (a):* the halo mass against  $V/\sigma$ . *Panel (b):* the number of halo members against  $V/\sigma$ . *Panel (c):* the halo mass against the cold gas fraction. *Panel (d):* the number of halo members against the cold gas fraction.

1972; Quilis et al. 2000), which may induce a star-gas misalignment. Fig. 9 shows the properties of a typical misaligned galaxy in a cluster environment. The panel in the middle shows the infalling trajectory of this galaxy by fixing the cluster center (X mark). The virial radius ( $R_{200}$ ) of the cluster at Stage 1 is marked with a shaded region. The PA offset (misalignment angle), shown in the color key dramatically changes from negli-

gible values (blue) outside of the cluster to high values (red) inside.

The small-inset panels show the gas velocity maps of the galaxy along the trajectory. The gas rotation axis (black arrow) quickly changes once the galaxy falls inside the cluster. The most dramatic change in the PA offset appears at Stage 3, when the first pericenter pass of the galaxy occurs. The first pericenter pass is widely considered to be the place where the most dramatic ram

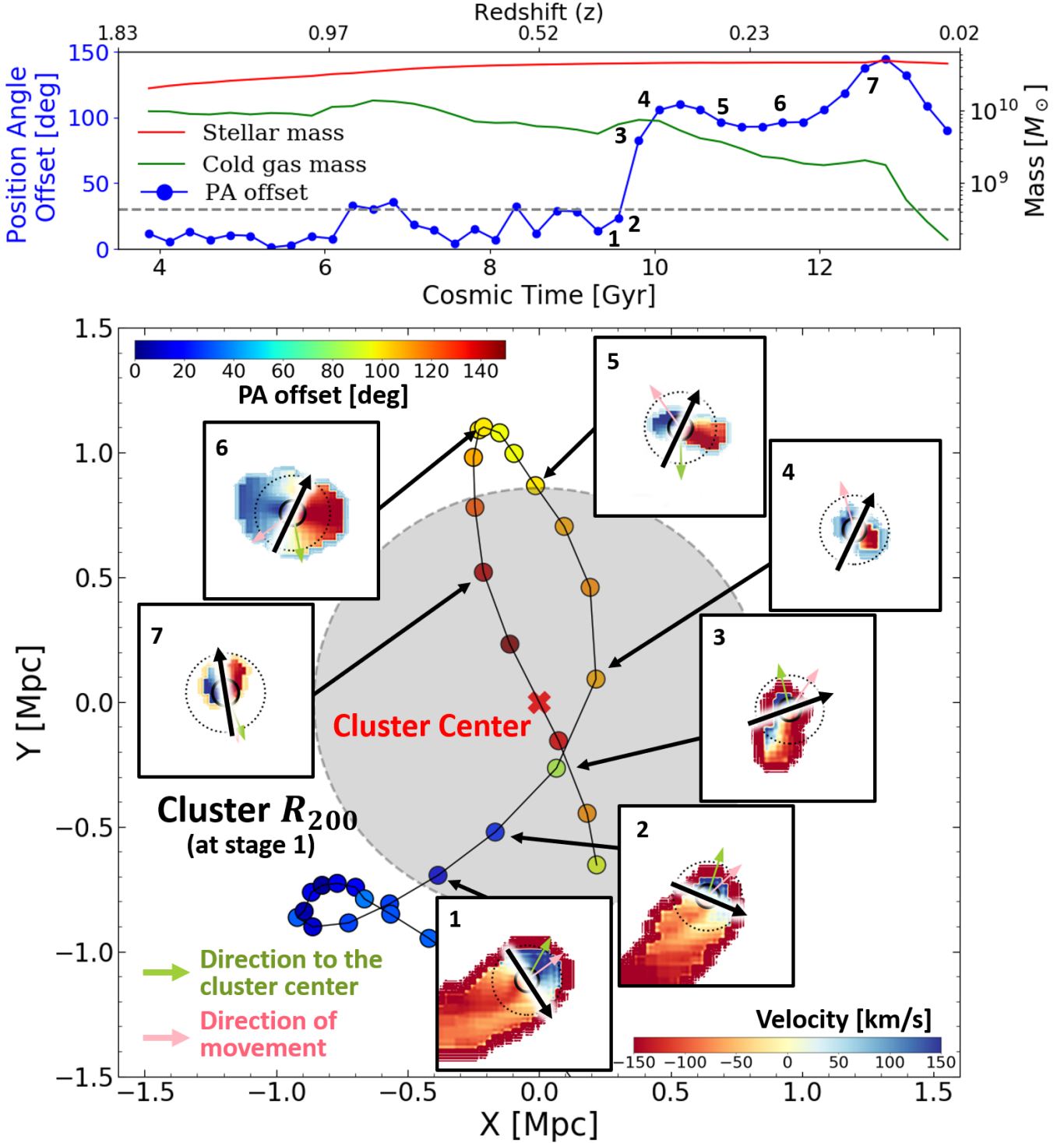


**Figure 9.** A typical misaligned galaxy in a cluster environment. We numbered particular snapshots along the trajectory (Stages 1 – 7). *Top*: the properties of the galaxy. While stellar mass (red) does not change significantly inside the cluster, the cold gas mass (green) decreases rapidly due to ram pressure stripping. The strong gas stripping seems to be accompanied by an increasing PA offset (blue). *Bottom*: the infalling trajectory of the galaxy. The cluster center is fixed and marked with a red X mark. The virial radius ( $R_{200}$ ) at Stage 1 is expressed by the gray shade region. Each point represents the position of the galaxy, and is color-coded by the PA offset. The PA offset dramatically changes when the galaxy passes the first pericenter (Stage 3). *Inset panels*: the projected cold gas map of the galaxy. The measured gas rotation axis is expressed in a black arrow. The green and the pink arrows indicate the direction to the cluster center and the galaxy's motion, respectively. While the stripped gas tail extends in the opposite direction to the galaxy's motion (ram pressure), the gas disk wobbles as it makes the misalignment.

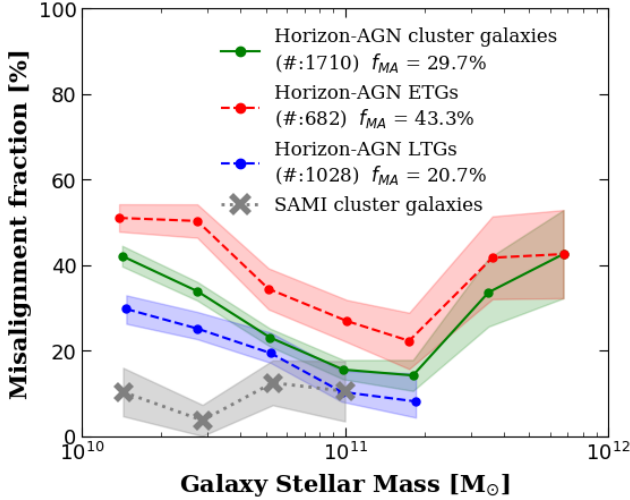


**Figure 10.** Same as Fig. 7, but for cluster galaxies. Each point contains at least 5 galaxies, and shadowed regions show the  $1\sigma$  error of the mean of a binomial distribution. While the same mass trend is visible among the cluster galaxies for  $M_* \gtrsim 10^{11}$ , it shows a reverse mass trend at  $M_* \lesssim 10^{11}$  against Fig. 7.

pressure stripping occurs because both the density of the ICM and the galaxy’s speed of motion attain maximal values along the trajectory.

Along with changes of the gas rotation axis, the amount of gas also systematically decreases due to ram pressure stripping, as shown in the top panel (green line). Meanwhile, stellar components are not affected much by the cluster environment. From Stages 1 through 7, the stellar mass of the galaxy (shown in red in the top panel) hardly changes, whereas the gas mass decreases roughly by a factor of four. In addition, using the Yonsei Zoom-in Cluster Simulation (YCiCS; Choi & Yi 2017), Lee et al. (2018) found that the spin direction of the stellar rotating disk inside a cluster does not change much during its pericenter passage. We also found the same result in Horizon-AGN cluster galaxies. An independent study based on the Illustris simulation also suggested that gas stripping contributes significantly to the misalignment (Starkenburg et al. 2019). Therefore, it seems that *the star-gas misalignment in cluster galaxies experiencing strong gas stripping comes mainly from the “wobbling” gas disk*

If the misalignment in the cluster environment is largely due to the ram pressure effect, it is expected to be correlated with halo mass and galaxy mass: a larger halo mass boosts the ram pressure effect while a larger galaxy mass counteracts it. In Fig. 8, we see that the misalignment fraction shows a clear positive trend with halo mass. Using YCiCS, Jung et al. (2018) found that ram pressure is at work even in small group size halos,

albeit at a low level. Consequently, the gradual change of the misalignment fraction of cluster galaxies with respect to cluster mass is physically expected.

Fig. 10 checks the mass trend for *cluster* galaxies in the same manner as Fig. 7. A positive mass trend is visible among the cluster galaxies in the simulation when  $M_* \gtrsim 10^{11}$ . We may interpret this as a result of the mass-morphology relation, as for Fig. 7. However, the mass trend is reversed in the simulation galaxies at  $M \lesssim 10^{11} M_\odot$ .

Horizon-AGN cluster galaxies do not show a morphology dependence in their mass trend; hence the inverse-mass trend (green line) cannot be a result of different mass trends of ETGs and LTGs, which was the argument used for the whole set of (dominantly non-cluster) galaxies in Fig. 7. We instead interpret this as a result of the lower restoring force of lower-mass galaxies acting against the ram pressure inside the cluster. These are all consistent with expectations based on the impact of ram pressure.

The origin of the wobbling of the gas disks of cluster galaxies is unclear. The direct blow-away effect of ram pressure may change the gas distribution and possibly its velocity map as well, but most of the effect would be visible in the outskirts of the galaxy, where gas density is too low to be decisive on the measurement of the gas disk kinematics.

#### 4.1.2. Phase-space analysis and misalignment

The location of cluster galaxies in the phase-space diagram is known to be closely linked with the infalling history (e.g., Gill et al. 2005; Oman et al. 2013; Rhee et al. 2017) and the star formation activity of galaxies (e.g., Hernández-Fernández et al. 2014; Muzzin et al. 2014; Oman & Hudson 2016; Rhee et al. 2017; Owers et al. 2019).

We plot a phase-space diagram in Fig. 11-(a) using the clustocentric velocities and distances of galaxies. The distance axis is normalized by the virial radius of cluster ( $R_{200}$ ), and the 3D clustocentric velocity axis is normalized by the spatial velocity dispersion of the cluster ( $\sigma_{3D}$ ). We define the center of the dark matter halo as the cluster center. The cluster galaxies are color-coded based on their PA offset, and their size scales with this offset. Overall, the values of PA offset and misalignment fraction are found to be higher in the cluster’s central region than in the outskirts. Fig. 11-(b) shows a 2D histogram of the misalignment fraction based on Panel (a) by stacking the recent 20 snapshots ( $z = 0 - 0.5$ ). The regions inside the virial radius ( $R_{200}$ ) have higher misalignment fractions than those in the outskirts. Also, the “backsplash region” (BS) is found to have a higher

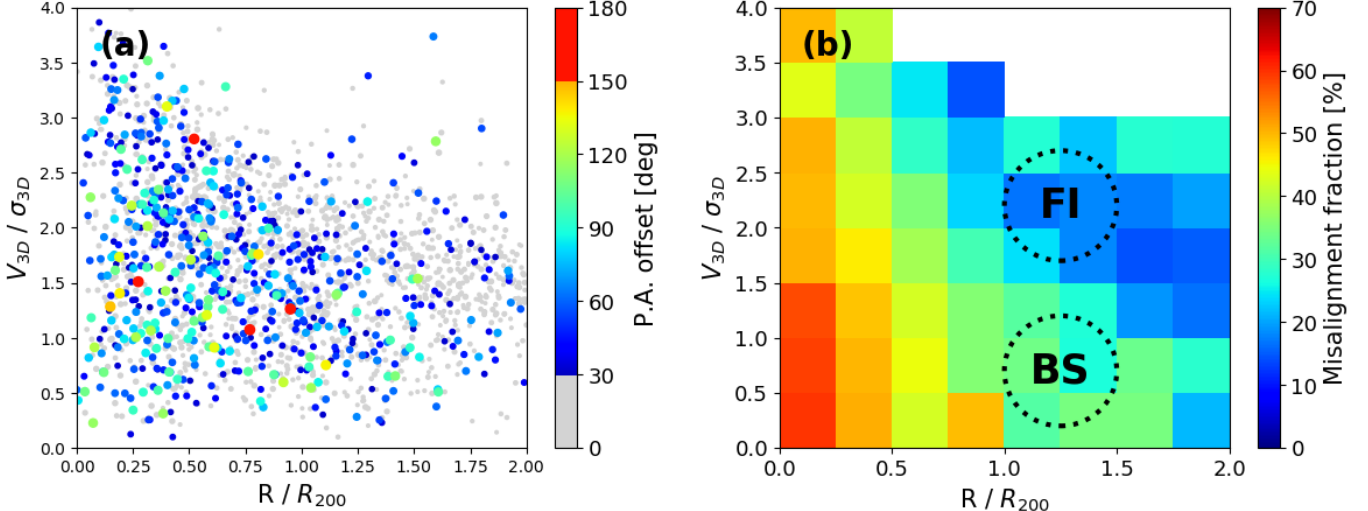


**Figure 11.** Phase-space analysis of Horizon-AGN cluster galaxies. *Panel (a)*: the phase-space diagram of cluster galaxies. While aligned galaxies are expressed as gray points, the misaligned galaxies (PA offset  $> 30^\circ$ ) are color-coded based on their PA offset. Their size scales with their PA offset. *Panel (b)*: 2D histogram of the misalignment fraction of cluster galaxies in the phase-space diagram. The central regions have a higher misalignment fraction than those at the outskirts. Each pixel contains at least 20 galaxies. The galaxies that have not fallen into the cluster (“first infaller”) and the “backsplash” galaxies are roughly populated in the regions marked as “FI” and “BS” and associated contours. (Rhee et al. 2017).

misalignment fraction than the “first infalling region” (FI). (c.f., Rhee et al. 2017).

A similar trend is found in Jaffé et al. (2018). They displayed jellyfish galaxies in the phase-space diagram using the data from Poggianti et al. (2016) and the GASP survey (Penoyre et al. 2017). Jellyfish galaxies are referred to the galaxies having star formation in the stripped gas, which can only be observed when fairly dense cold gas is stripped out. Jaffé et al. (2018) reported that many jellyfish galaxies are found on the left side of the phase-space diagram, which agrees well with Fig. 11-(b). Also, Bryant et al. (2019) have found a direct evidence that the cluster environment can cause misalignment via gas stripping.

#### 4.2. Discrepancy between observations and simulations

As mentioned at the beginning of Section 4.1, an outstanding issue is that there is a serious discrepancy between observations and simulations regarding the misalignment fraction among cluster galaxies. While observations show no clear differences between cluster galaxies and field galaxies, Horizon-AGN shows elevated by a factor of 3 among cluster galaxies. We find it difficult to reconcile this tension.

We used a different halo mass range from that of SAMI, because Horizon-AGN does not have as many massive clusters as in the observation. Given that the misalignment fraction shows a clear positive trend with halo mass (Fig. 8), we expect the misalignment fraction to be increased, if we had as many massive clusters as

in the observation. Therefore, there would still be large discrepancy between the simulation and SAMI.

One possibility is that the spatial and mass resolutions of gas cells in the simulations are too poor to model the relevant gas distribution within cluster galaxies. The spatial resolution of Horizon-AGN ( $\sim 1$  kpc) is comparable to those of the other cosmological large-volume simulations of galaxy formation; e.g., Illustris (Vogelsberger et al. 2014) and Eagle (Schaye et al. 2015). However, it is still much larger than the vertical scale of galactic thin disks. With such a low resolution, we cannot resolve the detailed features of multiphase ISM and the Kelvin-Helmholtz instability, which happens at the front of galactic disk and the ICM (See also Jung et al. 2018).

Cluster galaxies are relatively poorer in gas content than field galaxies. When the amount of gas is so small, it is more difficult to model properly the thin gas disk as found in real galaxies. When such a small amount of gas is spread out in larger areas in the simulated galaxies, it might be more vulnerable to the ram pressure stripping. This might be related with the so-called “satellite overquenching problem” (Kimm et al. 2009).

Another possibility is that the method used to measure gas properties differs between observations and simulations. In our simulational analysis, we derived the gas disk properties by measuring the net angular momentum of gas within an effective radius, naively counting all gas cells/particles. In reality, however, observers measure the gas properties taking into account column

density, optical depth, extinction, etc. The definition of “cold gas” also matters. IFS typically determines the gas rotation axis based on the *ionized* gas distribution, whereas we utilized the whole cold gas (by the density-temperature criterion) distribution in the Horizon-AGN simulation (Section 2.4). The ionized gas of a galaxy could be misaligned from the total cold gas distribution for the following argument. Compared to the neutral gas, ionized gas must be geographically more closely associated with young stars, and young stars form in dense regions which are less affected by environmental effects such as ram pressure. Moreover, PA offset can be measured differently depending on where it is based, as a significant number of galaxies show different values of PA offset at different radial distances. When we changed the position of measurement in the simulation data from  $1 R_{\text{eff}}$  to  $2 R_{\text{eff}}$ , however, its impact upon the result was found to be negligible (the misalignment fraction became 10% instead of 11%). It is necessary to measure gas in the simulations more realistically by first generating mock images of galaxies and following the same measurement techniques that were used by the observers.

Neither of these possibilities fall within the scope of the current investigation, but both are interesting subjects for future research.

## 5. SUMMARY

We used the Horizon-AGN simulation to investigate the *properties* of star-gas misaligned galaxies. Overall, Horizon-AGN reproduced the observed/expected misalignment features in terms of morphology ( $V/\sigma$ ), cold gas fraction, and galaxy mass, but not the observed diversity found in different. We summarize our results and their implications here.

We have compared the misaligned galaxies from Horizon-AGN and SAMI, applying a stellar mass cut and a cold gas detection limit. Horizon-AGN reproduced the PA offset distribution of SAMI galaxies remarkably well. However, Horizon-AGN did not reproduce the small peaks at 90- and 180-degrees observed by SAMI. It is probable that the spatial resolution of Horizon-AGN is insufficient to resolve such small peaks or that the resolution causes small peaks dissolve to more quickly in simulations than in real galaxies.

ETGs are found to show larger misalignment fractions both in SAMI and Horizon-AGN. Horizon-AGN galaxies with lower values of  $V/\sigma$  (kinematic morphology indicator) tend to have higher misalignment fractions and higher values of PA offsets. While the dynamical settling time depending on ellipticity can partially explain this phenomenon, it is insufficient to explain all of it.

We found in the Horizon-AGN galaxies that kinematic morphology and gas fraction independently affect the misalignment fraction. Smaller values of the two parameters ( $V/\sigma$  and cold gas fraction) correspond to higher misalignment fractions. Galaxies with higher gas fractions can sustain their gas kinematics more easily against external gas accretion. Moreover, a massive gas disk can attract a stellar disk faster, resulting in a quicker decay of misalignment.

The misalignment fraction is also seemingly affected by stellar mass. However, we have found that this trend largely arises from the fact that more massive galaxies tend to be earlier in type with lower in gas content.

One outstanding discrepancy between observations (SAMI) and simulations (Horizon-AGN) was found in dense (cluster) environments. Observations found no clear difference in misalignment fraction between field and cluster environments, whereas Horizon-AGN found a factor of three higher values in cluster galaxies regardless of morphology. This enhanced misalignment fraction in Horizon-AGN also shows a strong correlation with halo mass. We found that star-gas misalignment in cluster galaxies experiencing strong ram pressure stripping comes mainly from the wobbling gas disk. We suspect that the low spatial resolution of current large-volume simulations and/or the use of different gas measurement techniques contribute significantly to the discrepancy.

We will investigate the *origin and evolution* of misaligned galaxies, identifying different channels of misalignment formation and quantifying their levels of significance, in the follow-up paper, Paper II (Khim et al. in prep). We will also measure the lifetimes of star-gas misalignment for different types of galaxies.

## ACKNOWLEDGMENTS

SKY acted as the corresponding author and acknowledges support from the Korean National Research Foundation (NRF-2017R1A2A05001116). DJK acknowledges support from Yonsei University through Yonsei Honors Scholarship. JJB acknowledges support of an Australian Research Council Future Fellowship (FT180100231). JBH is supported by an ARC Laureate Fellowship that funds Jesse van de Sande and an ARC Federation Fellowship that funded the SAMI prototype. MSO acknowledges the funding support from the Australian Research Council through a Future Fellowship (FT140100255). JvdS is funded under Bland-Hawthorn’s ARC Laureate Fellowship (FL140100278). Parts of this research were conducted by the Australian Research Council Centre of Excellence for All Sky Astrophysics in 3 Dimensions (ASTRO 3D), through project number CE170100013. This work relied on the HPC resources of the Horizon Cluster hosted by Institut d’Astrophysique de Paris. We warmly thank S. Rouben for running the cluster on which the simulation was post-processed.

This work is partially supported by the Spin(e) grant ANR-13-BS05-0005 of the French Agence Nationale de

la Recherche. The SAMI Galaxy Survey is based on observations made at the Anglo-Australian Telescope. The Sydney-AAO Multi-object Integral field spectrograph (SAMI) was developed jointly by the University of Sydney and the Australian Astronomical Observatory. The SAMI input catalogue is based on data taken from the Sloan Digital Sky Survey, the GAMA Survey and the VST ATLAS Survey. The SAMI Galaxy Survey is supported by the Australian Research Council Centre of Excellence for All Sky Astrophysics in 3 Dimensions (ASTRO 3D), through project number CE170100013, the Australian Research Council Centre of Excellence for All-sky Astrophysics (CAASTRO), through project number CE110001020, and other participating institutions. The SAMI Galaxy Survey website is <http://sami-survey.org/>

## REFERENCES

- Algolliy, D. G., Navarro, J. F., Abadi, M. G., et al. 2014, *MNRAS*, **437**, 3596
- Aubert, D., Pichon, C., & Colombi, S. 2004, *MNRAS*, **352**, 376
- Aumer, M. & White, S. D. M. 2013, *MNRAS*, **428**, 1055
- Balcells, M. & Quinn, P. J. 1990, *ApJ*, **361**, 381
- Barnes, J. E. & Hernquist, L. 1996, *ApJ*, **471**, 115
- Barrera-Ballesteros, J. K., Falcón-Barroso, J., García-Lorenzo, B., et al. 2014, *A&A*, **568**, A70
- Barrera-Ballesteros, J. K., García-Lorenzo, B., Falcón-Barroso, J., et al. 2015, *A&A*, **582**, A21
- Bekki, K. 1998, *ApJ*, **499**, 635
- Bertola, F., Buson, L. M., & Zeilinger, W. W. 1992, *ApJ*, **401**, L79
- Bournaud, F. & Combes, F. 2003, *A&A*, **401**, 817
- Brook, C. B., Governato, F., Quinn, T., et al. 2008, *ApJ*, **689**, 678
- Bryant, J. J., Croom, S. M., van de Sande, J., et al. 2019, *MNRAS*, **483**, 458
- Bryant, J. J., Owers, M. S., Robotham, A. S. G., et al. 2015, *MNRAS*, **447**, 2857
- Bundy, K., Scarlata, C., Carollo, C. M., et al. 2010, *ApJ*, **719**, 1969
- Bureau, M. & Chung, A. 2006, *MNRAS*, **366**, 182
- Choi, H. & Yi, S. K. 2017, *ApJ*, **837**, 68
- Chung, A., Koribalski, B., Bureau, M., & van Gorkom, J. H. 2006, *MNRAS*, **370**, 1565
- Coccato, L., Fabricius, M., Morelli, L., et al. 2015, *A&A*, **581**, A65
- Coccato, L., Morelli, L., Corsini, E. M., et al. 2011, *MNRAS*, **412**, L113
- Conselice, C. J. 2006, *MNRAS*, **373**, 1389
- Cortese, L., Fogarty, L. M. R., Bekki, K., et al. 2016, *MNRAS*, **463**, 170
- Crocker, A. F., Jeong, H., Komugi, S., et al. 2009, *MNRAS*, **393**, 1255
- Croom, S. M., Lawrence, J. S., Bland-Hawthorn, J., et al. 2012, *MNRAS*, **421**, 872
- Davis, T. A., Alatalo, K., Sarzi, M., et al. 2011, *MNRAS*, **417**, 882
- Davis, T. A. & Bureau, M. 2016, *MNRAS*, **457**, 272
- De Rijcke, S., Dejonghe, H., Zeilinger, W. W., & Hau, G. K. T. 2004, *A&A*, **426**, 53
- Dressler, A. 1980, *ApJ*, **236**, 351
- Dubois, Y., Peirani, S., Pichon, C., et al. 2016, *MNRAS*, **463**, 3948

- Dubois, Y., Pichon, C., Welker, C., et al. 2014, *MNRAS*, **444**, 1453
- Emsellem, E., Cappellari, M., Krajnović, D., et al. 2007, *MNRAS*, **379**, 401
- Gill, S. P. D., Knebe, A., & Gibson, B. K. 2005, *MNRAS*, **356**, 1327
- Gómez, P. L., Nichol, R. C., Miller, C. J., et al. 2003, *ApJ*, **584**, 210
- Gunn, J. E. & Gott, III, J. R. 1972, *ApJ*, **176**, 1
- Hernández-Fernández, J. D., Haines, C. P., Diaferio, A., et al. 2014, *MNRAS*, **438**, 2186
- Hernquist, L. & Barnes, J. E. 1991, *Nature*, **354**, 210
- Ilbert, O., Salvato, M., Le Floc'h, E., et al. 2010, *ApJ*, **709**, 644
- Jaffé, Y. L., Poggianti, B. M., Moretti, A., et al. 2018, *MNRAS*, **476**, 4753
- Jin, Y., Chen, Y., Shi, Y., et al. 2016, *MNRAS*, **463**, 913
- Jung, S. L., Choi, H., Wong, O. I., et al. 2018, *ApJ*, **865**, 156
- Kannappan, S. J. & Fabricant, D. G. 2001, *AJ*, **121**, 140
- Katkov, I. Y., Sil'chenko, O. K., Chilingarian, I. V., Uklein, R. I., & Egorov, O. V. 2016, *MNRAS*, **461**, 2068
- Kimm, T., Somerville, R. S., Yi, S. K., et al. 2009, *MNRAS*, **394**, 1131
- Komatsu, E., Smith, K. M., Dunkley, J., et al. 2011, *ApJS*, **192**, 18
- Krajnović, D., Weilbacher, P. M., Urrutia, T., et al. 2015, *MNRAS*, **452**, 2
- Kuijken, K., Fisher, D., & Merrifield, M. R. 1996, *MNRAS*, **283**, 543
- Lagos, C. d. P., Padilla, N. D., Davis, T. A., et al. 2015, *MNRAS*, **448**, 1271
- Lee, J., Kim, S., Jeong, H., et al. 2018, *ApJ*, **864**, 69
- Muzzin, A., van der Burg, R. F. J., McGee, S. L., et al. 2014, *ApJ*, **796**, 65
- Oman, K. A. & Hudson, M. J. 2016, *MNRAS*, **463**, 3083
- Oman, K. A., Hudson, M. J., & Behroozi, P. S. 2013, *MNRAS*, **431**, 2307
- Owers, M. S., Allen, J. T., Baldry, I., et al. 2017, *MNRAS*, **468**, 1824
- Owers, M. S., Hudson, M. J., Oman, K. A., et al. 2019, *ApJ*, **873**, 52
- Penoyre, Z., Moster, B. P., Sijacki, D., & Genel, S. 2017, *MNRAS*, **468**, 3883
- Pizzella, A., Corsini, E. M., Vega Beltrán, J. C., & Bertola, F. 2004, *A&A*, **424**, 447
- Poggianti, B. M., Fasano, G., Omizzolo, A., et al. 2016, *AJ*, **151**, 78
- Puerari, I. & Pfenniger, D. 2001, *Ap&SS*, **276**, 909
- Quilis, V., Moore, B., & Bower, R. 2000, *Science*, **288**, 1617
- Rhee, J., Smith, R., Choi, H., et al. 2017, *ApJ*, **843**, 128
- Rodríguez-Gómez, V., Sales, L. V., Genel, S., et al. 2017, *MNRAS*, **467**, 3083
- Rubin, V. C., Graham, J. A., & Kenney, J. D. P. 1992, *ApJ*, **394**, L9
- Sarzi, M., Falcón-Barroso, J., Davies, R. L., et al. 2006, *MNRAS*, **366**, 1151
- Schaye, J., Crain, R. A., Bower, R. G., et al. 2015, *MNRAS*, **446**, 521
- Schweizer, F., Whitmore, B. C., & Rubin, V. C. 1983, *AJ*, **88**, 909
- Serra, P., Oser, L., Krajnović, D., et al. 2014, *MNRAS*, **444**, 3388
- Snyder, G. F., Torrey, P., Lotz, J. M., et al. 2015, *MNRAS*, **454**, 1886
- Starkenburg, T. K., Sales, L. V., Genel, S., et al. 2019, *ApJ*, **878**, 143
- Sweet, S. M., Drinkwater, M. J., Meurer, G., et al. 2016, *MNRAS*, **455**, 2508
- Teyssier, R. 2002, *A&A*, **385**, 337
- Thakar, A. R. & Ryden, B. S. 1996, *ApJ*, **461**, 55
- Torrey, P., Vogelsberger, M., Sijacki, D., Springel, V., & Hernquist, L. 2012, *MNRAS*, **427**, 2224
- Tweed, D., Devriendt, J., Blaizot, J., Colombi, S., & Slyz, A. 2009, *A&A*, **506**, 647
- Ulrich, M.-H. 1975, *PASP*, **87**, 965
- van de Sande, J., Lagos, C. D. P., Welker, C., et al. 2019, *MNRAS*, **484**, 869
- van de Voort, F., Davis, T. A., Kereš, D., et al. 2015, *MNRAS*, **451**, 3269
- van Gorkom, J. H., Schechter, P. L., & Kristian, J. 1987, *ApJ*, **314**, 457
- Vogelsberger, M., Genel, S., Springel, V., et al. 2014, *MNRAS*, **444**, 1518
- Whitmore, B. C., Lucas, R. A., McElroy, D. B., et al. 1990, *AJ*, **100**, 1489